Journal of Asian Earth Sciences 195 (2020) 104378

Contents lists available at ScienceDirect

Journal of Asian Earth Sciences

journal homepage: www.elsevier.com/locate/jseaes

Seismic velocity structure beneath the Western Solomon Islands from the joint inversion of receiver functions and surface-wave dispersion curves

Chin-Shang Ku[a,b], Yu-Ting Kuo[b], Bor-Shouh Huang[a,b], Yue-Gau Chen[a,b,c,d], Yih-Min Wu[a,b,e,*]

[a] Department of Geosciences, National Taiwan University, Taipei 10617, Taiwan
[b] Institute of Earth Sciences, Academia Sinica, Taipei 11529, Taiwan
[c] Research Center for Environmental Changes, Academia Sinica, Taipei 11529, Taiwan
[d] Center for Sustainability Science, Academia Sinica, Taipei 11529, Taiwan
[e] NTU Research Center for Future Earth, National Taiwan University, Taipei 10617, Taiwan

ARTICLE INFO

Keywords:
Solomon Islands
Receiver functions
Surface-wave dispersion curve
Joint inversion

ABSTRACT

An M_W 8.1 earthquake occurred in 2007 and induced a tsunami that hit the Western Solomon Islands and caused casualties. This motivated us to deploy a seismic network around the rupture zone of the 2007 event. To investigate the seismic velocity structure of the Western Solomon Islands, we select seismograms of teleseismic events recorded by our seismic network. Joint inversion of P-wave receiver functions and surface-wave group velocity dispersion curves is used to estimate station-based 1-D velocity models. The resulting velocity models show a highly variable crustal structure across the region. The Moho depths beneath the stations range from 25 to 40 km. A low-velocity zone (LVZ) is observed at most seismic stations in this work. Our study provides preliminary station-based seismic velocity models for the study region, and more stations will be deployed in the continuing project. An integrated 3-D velocity model will be determined in the future.

1. Introduction

The Solomon Islands is located in the southwestern Pacific Ocean, which is a complex boundary between the Pacific, Australian, and Woodlark plates (Fig. 1). Two large earthquakes occurred in 2007 and 2010, and both shock the Western Solomon Islands. The M_W 8.1 event of April 1, 2007, was the largest instrumentally recorded earthquake in the Solomon Islands (Fritz and Kalligeris, 2008; Taylor et al., 2008; Chen et al., 2009; Miyagi et al., 2009). The rupture zone of the 2007 event was approximately 245 km in length and extended from the San Cristobal Trench and extends to the New Britain Trench (Taylor et al., 2008). After three years, an M_W 7.1 earthquake occurred and triggered the tsunami that hit the local area (Newman et al., 2011; Kuo et al., 2016). Both events caused injuries and deaths. Our group then planned to deploy instruments around the rupture zone of the 2007 event to perform seismological and geological investigations (Kuo et al., 2016; Ku et al., 2018). Valuable data have been recorded from this project, and the recording is still in progress.

Subduction zones are areas where new continental crust is generated; however, the discrepancy in the compositions of the average continental crust and that beneath island arcs is still unclear (Taylor, 1967; Janiszewski et al., 2013; Schlaphorst et al., 2018). The Moho discontinuity, which is the boundary between the crust and the mantle, provides much information about the tectonic processes around subduction zones. The local seismic network deployed in the Western Solomon Islands provides us with an excellent opportunity to study the seismic velocity structure and the Moho depth variation around the study area. The seismic velocity structure is an essential element for seismological studies (e.g., hypocenter locations and focal mechanism determination). Ku et al. (2018) used ambient noise recorded at seismic stations and applied the genetic algorithm to invert an average 1-D velocity model for the Western Solomon Islands (WSOLOCrust). Although the WSOLOCrust model obtained better travel time residuals for local earthquakes compared to other 1-D models, it still has limited constraints regarding the deeper seismic velocity structure because it employs ambient noise. The WSOLOCrust model also cannot provide lateral variations in the structure. Therefore, it is necessary to improve the seismic velocity model.

The receiver function method has been applied widely in the past few decades to study the crust and upper mantle structure. Langston (1979) originally developed the receiver function method, which was later improved by various groups in different aspects, such as spectral estimation and velocity inversion. (Owens et al., 1988; Ammon et al., 1990; Cassidy, 1992; Shibutani et al., 1996; Sambridge, 1999; Park and

* Corresponding author at: Department of Geosciences, National Taiwan University, Taiwan, No. 1, Sec. 4, Roosevelt Road, Taipei 10617, Taiwan.
E-mail address: drymwu@ntu.edu.tw (Y.-M. Wu).

https://doi.org/10.1016/j.jseaes.2020.104378
Received 29 November 2019; Received in revised form 23 April 2020; Accepted 23 April 2020
Available online 28 April 2020
1367-9120/

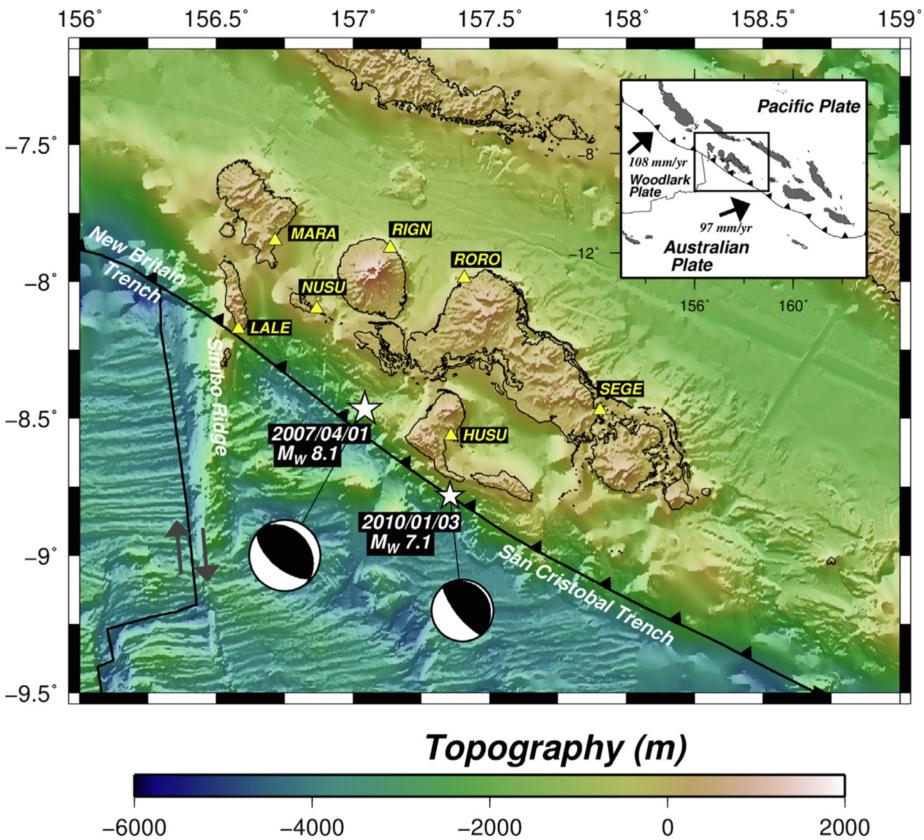

Fig. 1. The map displays the bathymetry and the distribution of seismic stations (yellow triangles) in our study area. The inset shows the plate tectonic setting around the Solomon Islands. The triple junction is located where the Pacific, Australian, and Woodlark plate boundaries intersect. Two white stars and related beach balls indicate the epicenters and focal mechanisms of the earthquakes that occurred in 2007 and 2010, respectively. (For interpretation of the references to colour in this figure legend, the reader is referred to the web version of this article.)

Levin, 2000). Briefly, receiver functions use the seismograms of teleseismic earthquakes that sample the Earth along the travel path. The receiver function, as a response to the Earth's structure beneath the receiver site, can be estimated by deconvolving the vertical component from the horizontal component seismogram. However, the receiver function is sensitive to the relative arrival times of the converted phases from discontinuities beneath the receiver site but has poor constraints on the absolute velocities. In contrast, surface-wave dispersion data are sensitive to the true velocity structure but are less sensitive to the sharp velocity contrasts between the layers beneath a station. Joint inversion benefits both methods. Thus, the combination of both data sets to invert the velocity model has been popular in recent decades (e.g., Bodin et al., 2012; Julià et al., 2000, 2003; Shen et al., 2012; Chen and Niu, 2016; Wang et al., 2019). We collect data from teleseismic events to perform joint inversion of receiver functions and surface-wave dispersion curves.

To better resolve the structure of the crust and upper mantle in the Western Solomon Islands, we analyze the receiver functions and surface-wave dispersion curves from the teleseismic data. We calculate the velocity models from joint inversion of the receiver functions and surface-wave dispersion curves. The Moho depth variations and preliminary station-based seismic velocity models of the Western Solomon Islands are proposed for the first time in this study.

2. Data and data processing

Data from seven broadband seismic stations are used for the receiver function analysis and surface-wave dispersion curve measurements. Seismic stations were deployed around the rupture zone of the 2007 Solomon earthquake (Fig. 1). A high-resolution recorder (Q330S; Kinemetrics, Inc., USA) and a broadband sensor (Trillium 120PA; Nanometrics, Inc., Canada) are equipped at each station. Different numbers of events are used at each station due to the different operating periods. Information about the seismic stations and the number of events used at each station can be found in Table S1.

2.1. Receiver function analysis

For receiver function analysis, we select seismograms for teleseismic events ($M_W > 5.5$) with epicentral distances from 30° to 90° recorded at our seismic stations. Only events with a clear P-phase are selected for this study. The horizontal component seismograms are rotated to radial and transverse components. Three components of the seismograms are filtered using a Butterworth bandpass filter of 50 s to 2 Hz. All the seismograms are resampled to 10 samples per second for the calculation efficiency. The waveform between 20 s before and 100 s after the P arrival for the receiver functions is calculated using a time-domain iterative deconvolution technique with a Gaussian factor of 1.5 (Ligorría and Ammon, 1999). A correlation coefficient matrix method (Tkalčić et al., 2011) is used to examine the results. For the purpose to obtain an average 1-D velocity model beneath each station (the azimuthal variations beneath each station will be left for further studies), at each station, the receiver functions for which the waveforms are not coherent with each other are removed.

Most teleseismic events occurred southeast and northwest of our network (Fig. 2a and e). Figure panels 2b and f show the results of station HUSU and SEGE, respectively, the receiver functions binned by the epicentral distance (5° bins with an increment of 3°) and back azimuths (5° bins with an increment of 10°). The results of other stations, please refer to Fig. S1. For each station, all the receiver functions are stacked to obtain a stacking receiver function to improve the signal-to-noise ratio. Stacking receiver functions with a window from −3 s to 10 s after the P arrival are used in joint inversion. The H-*k* method (Zhu and Kanamori, 2000) is also applied to all the receiver functions to estimate the crustal thickness (H) and the average P-wave to S-wave velocity ratio ($V_P/V_S = k$) of the crust beneath each station. A grid search is performed over a thickness range of 20–60 km and a V_P/V_S range of 1.5–2.0 at intervals of 0.5 km and 0.01, respectively. The

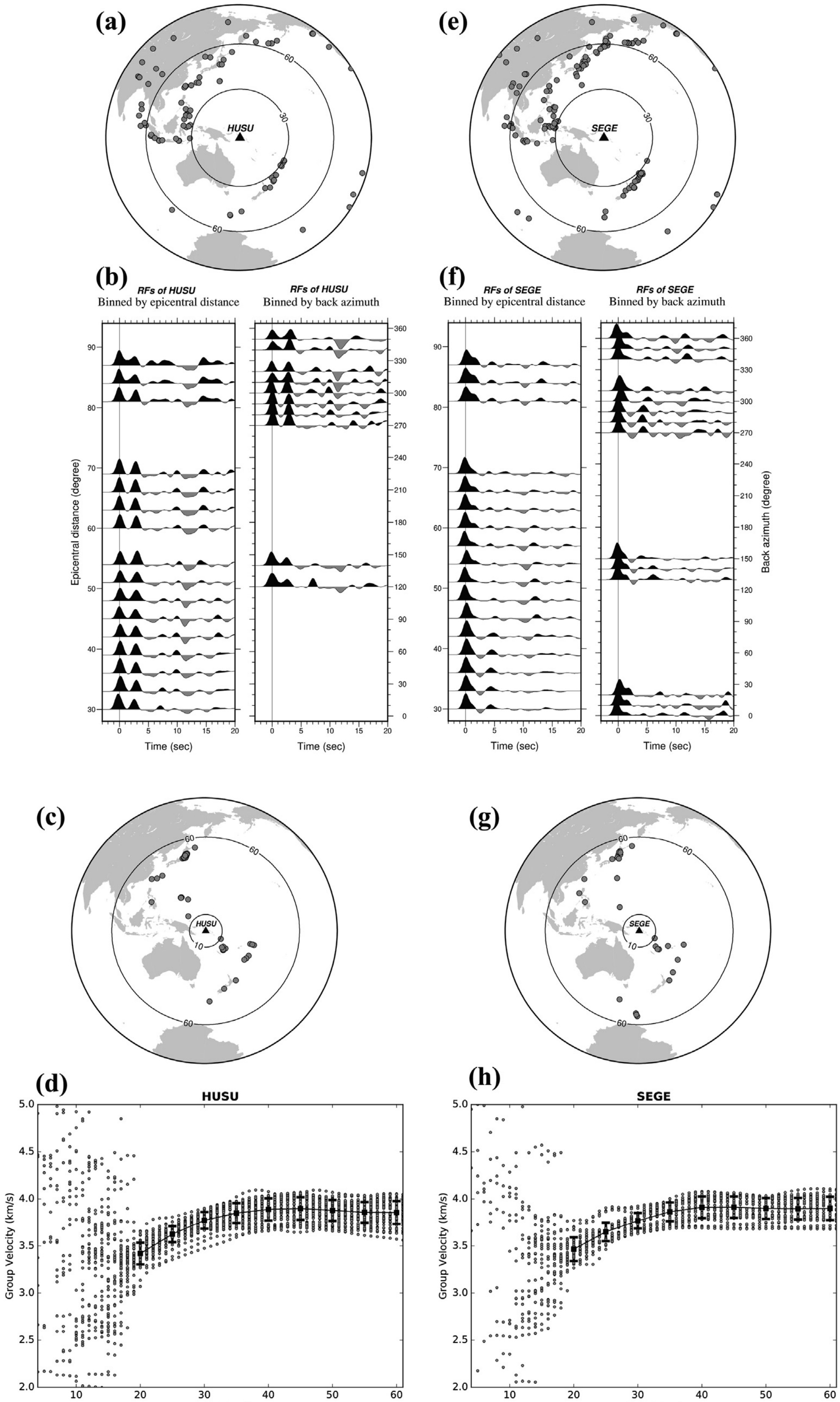

Fig. 2. Examples illustrating receiver functions and surface-wave group velocities for station HUSU (a-d) and SEGE (e-h). (a) The events used in the receiver function analysis for station HUSU (black triangle). The circles indicate the distribution of earthquakes. (b) All receiver functions at station HUSU. For better illustration, the waveforms have been stacked by epicentral distance (5° bins with an increment of 3°) and back azimuth (5° bins with an increment of 10°). Only stacking traces with more than five events in each bin are plotted. (c) The earthquake distribution (gray circles) at station HUSU (black triangle) for the Rayleigh-wave group velocity measurements. (d) The gray circles indicate the group velocity values of different events. The black squares and error bars indicate the average group velocity and one standard deviation of periods from 20 to 60 s with interval 5 s, respectively. (e-h) The corresponding results for station SEGE.

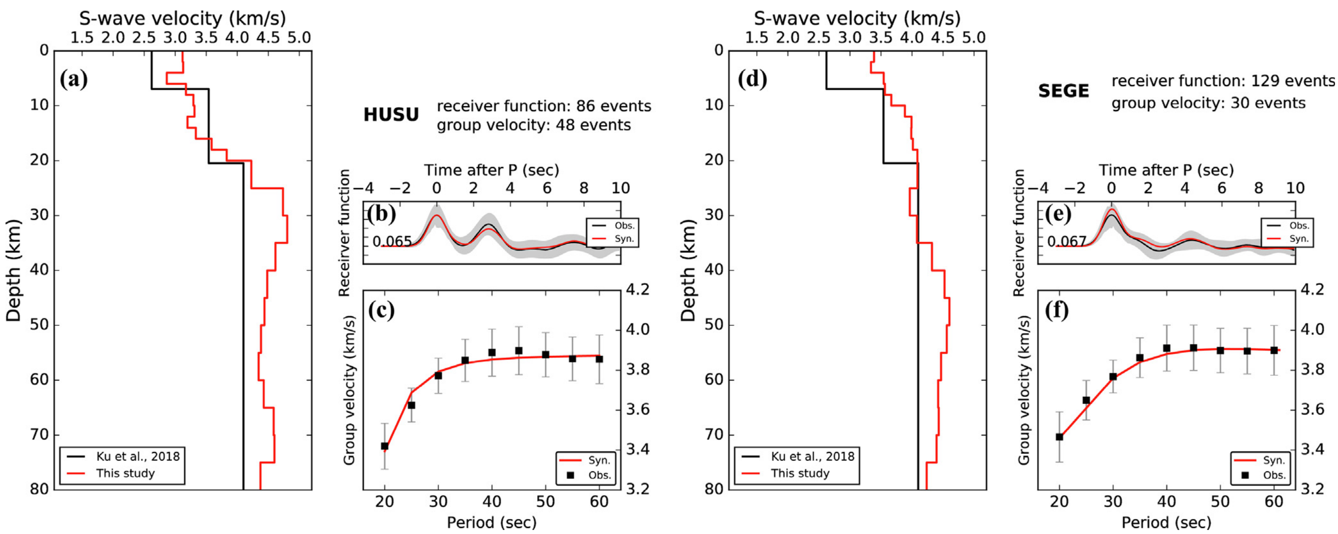

Fig. 3. Examples show the results of joint inversion for station HUSU (a-c) and SEGE (d-f). The numbers of events used in receiver function analysis and group velocity measurements are displayed at the top. (a) The red and black lines indicate our result and an average local model (Ku et al., 2018), respectively. (b) Comparison between the observed (black line) and synthetic (red line) receiver functions. The gray shadow represents one standard deviation of the observed receiver functions. The black numbers in front of waveforms indicate the average ray parameter of observed receiver functions. (c) The black squares and gray error bars indicate the average group velocities and one standard deviation with different periods, as the observed data. The red line indicates the synthetic group velocity. (d-f) The corresponding results for station SEGE. (For interpretation of the references to colour in this figure legend, the reader is referred to the web version of this article.)

average V_P is set to 6.0 km/s, and the weighting factor values of the Ps, PpPs, and PsPs/PpSs phases are 0.7, 0.2, and 0.1, respectively.

2.2. Rayleigh-wave group velocity measurements

For the Rayleigh-wave group velocity measurements, the vertical component of the seismograms of teleseismic events ($M_W > 6.0$) with the epicentral distances of 10°-60° are used. The mean, trend, and instrumental responses of the raw data are removed before calculating the group velocity. The group velocity of each event can be measured using the multiple filter technique (MFT; Dziewonski et al., 1969; Corchete et al., 2007; Ku et al., 2018). Figure panels 2c–d and 2g–h show examples of Rayleigh-wave group velocity measurements at stations HUSU and SEGE, respectively. The dispersion curves between different events are incoherent below 20 s because the teleseismic data have limited constraints in the shallower structure or lower periods (Fig. 2d and h). Thus, we average the group velocity of events from 20 to 60 s with an interval of 5 s for use in joint inversion. The black circles and error bars represent the average value and one standard deviation of the group velocities, respectively (Fig. 2d and h).

In this study, we obtain the 1-D velocity model by joint inversion of the stacking receiver function and the average group velocities for each station. More detailed studies of the complex structure (e.g., dipping layer and anisotropy) beneath each station will be left for further investigations.

3. Joint inversion and synthetic tests

The receiver function is sensitive to sharp velocity contrasts between layers beneath a seismic station. However, the receiver function has fewer constraints on the determination of the absolute velocity. In contrast, the surface-wave dispersion curve is more sensitive to the absolute average velocity over a certain range of depths. Thus, joint inversion can provide reliable velocity models (e.g., Bodin et al., 2012; Julià et al., 2000; Shen et al., 2012; Wang et al., 2019). Here, we apply the *joint96* program for joint receiver function and surface-wave dispersion curve to invert the 1-D velocity model; *joint96* is an iterative linearized least-squares inversion method from the software package Computer Programs in Seismology (CPS; Herrmann, 2013). CPS is also used to compute synthetic receiver functions and surface-wave dispersion curves.

In this study, the maximum depth of the velocity model is set to 80 km. The initial model consisting of a stack of thin layers with fixed thicknesses and uniform velocities is utilized. The model layers are 2 km thick at depths of 0–20 km and are 5 km thick at depths of 20–80 km. The initial model has a total of 22 layers. Herrmann et al. (2000) indicated that a *priori* information is required to stabilize the results of velocity models in the mantle. One possibility is to require the deepest layers in the model to be similar to predetermined values, such as in the PREM model (Dziewonski and Anderson, 1981). Thus, we refer to the PREM model to set the V_S, V_P/V_S ratio, and density of each layer to 4.6 km/s, 1.75, and 3.3 g/cm^3, respectively. Through trial and error tests, we find that eight iterations and an equal weighting on both data sets can provide a stable and efficient result. The iasp91 model (Kennett and Engdahl, 1991) and a model with a low-velocity or high-velocity layer are used in different tests. We subsequently apply three different models as the input forward model to generate the receiver functions and surface-wave group velocities as observed. Figure S2 shows the results of the inversions. From the synthetic tests, the inversion model can recover well with the iasp91, low-velocity, and high-velocity velocity models. Thus, the initial model used in the synthetic tests seems to be workable in this area, for which we do not have much prior knowledge. This approach has also been used in previous studies applying the *joint96* method (e.g., Rai et al., 2006; Acton et al., 2011; Gilligan et al., 2015, 2016). More descriptions of the synthetic tests can be found in Text S1.

4. Results

4.1. Station-based 1-D velocity models

Using the receiver functions and surface-wave dispersion curves, we apply the joint inversion described earlier to all the stations shown in Fig. 1. The 1-D velocity models of the stations are used to investigate variations in velocity throughout the area and to determine the Moho depth.

The inversion results of two stations are shown as examples in Fig. 3. An average 1-D velocity model (WSOLOCrust) calculated using

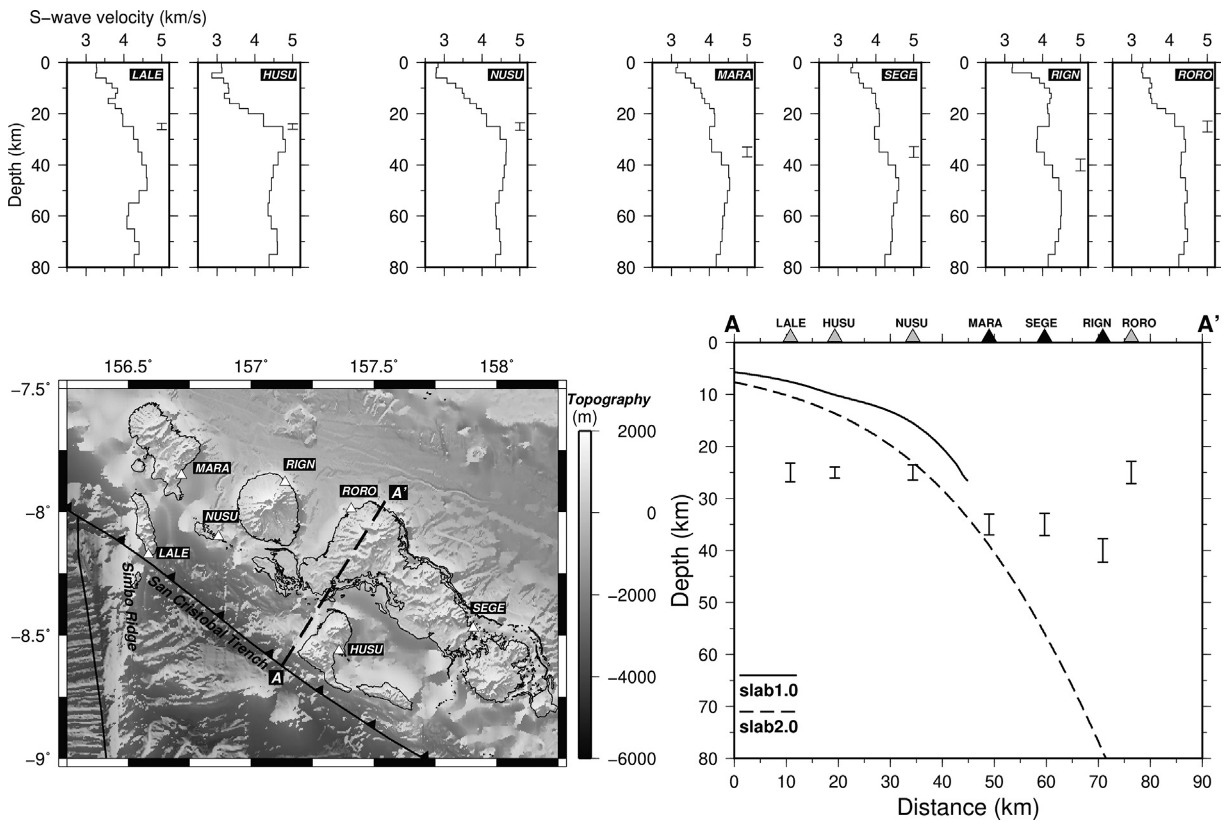

Fig. 4. The summary of 1-D velocity models and projection of our results onto a vertical profile (line AA′). (a) S-wave velocity models for each station. Black error bars show the possible MDR beneath stations. (b) The map shows the distribution of seismic stations (white triangles) and the location of line AA′ (dashed line). The results of all stations are projected onto line AA′. (c) This figure shows the vertical profile along line AA′. The solid and dashed lines indicate the Slab 1.0 and Slab 2.0 models, respectively. Triangles present the locations of the stations and the distances from the trench; three black triangles mark stations with greater Moho depths. Black error bars show the possible MDR, as in (a).

the ambient noise records was reported in the same area (Ku et al., 2018). The WSOLOCrust model has been proven to be able to obtain better travel time residuals compared to iasp91 (Kennett and Engdahl, 1991) or a local model extracted from CRUST 1.0 (Laske et al., 2013) for earthquakes occurring near the seismic array. We plot our results (red lines in Fig. 3a and d) together with the WSOLOCrust model (black lines in Fig. 3a and d), and more comparisons can be found in later discussion. The synthetic receiver functions fit well with the observations and are shown in Fig. 3b and e. The black line and gray zone represent the average receiver function as observed and one standard deviation, respectively; the number in front of the waveforms is the average ray parameter of the observed receiver function, and the red line indicates the synthetic receiver function (Fig. 3b and e). The fittings of the surface-wave dispersion curves are shown in Fig. 3c and f. The black squares and gray error bars indicate the average dispersion data and one standard deviation between the 20 s and 60 s periods, respectively, with an interval of 5 s; the red line indicates the synthetic dispersion curve (Fig. 3c and f). The results of the joint inversion from other stations can be found in Figure S3.

4.2. Possible Moho depth range and low-velocity zone

Following the method from previous studies that used joint inversion to investigate the crustal velocity structure (Gilligan et al., 2015, 2016), the Moho depth is picked from the 1-D S-wave velocity model at the base of the positive and steepest velocity gradient where $V_S > 4.2$ km/s. We use the selected Moho depth as the center of the error bar to present the possible Moho depth range (MDR), which is calculated according to the velocity change (VC) at the picked Moho depth. Here VC is defined as $VC = [V_{SL}-V_{SU}]/V_{SU}$, where V_{SL} and V_{SU} are the S-wave velocities of the lower and upper layers, respectively. For a better illustration, here, we define MDR = 1/VC/4.2; the larger the VC is, the smaller the possible MDR is. The low-velocity zone (LVZ) can be visually observed in most 1-D velocity models. Here, we search the LVZ above the picked Moho depth to focus on the crustal velocity structure. The LVZ starts at the depth where the VC is less than −2% and stops at the depth where the VC returns to being greater than zero. The MDR value and velocity reduction at each station can be found in Table S2. The V_P/V_S ratio of each layer can also be obtained during joint inversion, and V_P can be estimated in each layer. To help identify the Moho depth, we also apply the H-*k* method to the available receiver functions at each station to estimate the crustal thickness and average V_P/V_S ratio beneath the stations, and the results are shown in Figure S4. We examine the P- and S-wave velocity models obtained from joint inversion and compare them with the results from the H-*k* method, as shown in Figure S5. The black and gray error bars indicate the MDR and the LVZ from the 1-D velocity model, respectively; the dashed line indicates the Moho depth obtained from the H-*k* method. Only NUSU and RORO have no crustal LVZ. The Moho depths obtained by the different methods are close to each other at most stations except for RIGN and SEGE (Fig. S5). However, for these two stations, the locations of the best fit from the grid search of the H-*k* method are too close to the boundary of the searching domain (Fig. S4), and compared to other stations, a large part of the crustal LVZ is observed compared to other stations (Fig. S5). The H-*k* method is based on the theoretical arrival times of the converted phases to derive the crustal thickness and the average V_P/V_S ratio beneath a station. Thus, the H-*k* method used to investigate the crustal structure is prone to misinterpretation when a crustal low-velocity layer is present. Additionally, compared to the H-*k* method, joint inversion is more advanced in that we can obtain a full velocity model, which allows for a more detailed examination of the seismic velocity structure of the crust and uppermost mantle. Thus, we adopt the picked Moho depth obtained from the resulting joint inversion model for later discussion.

5. Discussion

The WSOLOCrust model constitutes two layers (upper and lower crust) and a half-space (uppermost mantle). The first discontinuous interface of the WSOLOCrust model that separates the upper and lower crust is at a depth of 6.9 km. From the resulting joint inversion models, MARA, RIGN, RORO, LALE, and NUSU reveal an apparent discontinuity at approximately 4–6 km (as shown in Fig. S3). The Moho of the WSOLOCrust model is at a depth of 20.4 km. However, the Moho depths from our results are deeper than 20.4 km (Fig. S5). Tetreault and Buiter (2014) reviewed future accreted terranes around the world and reported that island arcs have an average crustal thickness of 26 ± 6 km. The results obtained at most stations have close values of approximately 25 km. Moreover, considering the complex tectonic processes or structure in the study area, our results from joint inversion, as a form of station-based velocity models, could provide more lateral variations in the seismic velocity structure of the Western Solomon Islands.

A summary of the resulting model beneath each station is shown in Fig. 4a. Overall, we can visually separate the seven stations into two groups based on their Moho characters. The first group includes two stations, HUSU and NUSU. These two stations have the dominant Moho discontinuity and a significant increase in V_S of ~ 0.5 km/s at the Moho depth. The second group includes the remaining stations that do not display the dominant discontinuity. In the 1-D velocity models of these stations, the velocity change between the crust and mantle is smaller than that observed beneath the stations of the first group. Previous studies have also reported that the Moho might not be easy to acquire in many regions such as island arcs (e.g., Ewing et al., 1971; Boynton et al., 1979; Janiszewski et al., 2013).

For a better comparison of the Moho depth variations throughout the region, we select the direct line AA′, which is perpendicular to the strike of the trench (Fig. 4b), and project the MDR obtained at each station onto the vertical profile of line AA′ (Fig. 4c). The horizontal axis of Fig. 4c indicates the distance between the station and the trench; the black error bar indicates the MDR obtained at each station (as shown in Fig. 4a). Hayes et al. (2012) combined several data sets from active source and passive seismology to present the Slab 1.0 model of the global subduction zone geometries. As increasingly more data sets have become available in the past few years (e.g., the global distribution of earthquake locations, relocations, receiver functions, and tomography data), Hayes et al. (2018) further used available data sets to present a comprehensive subduction zone geometry model: Slab 2.0. Note that Slab 2.0 only uses the global distribution of earthquake locations and active source seismic data in the Solomon Islands area but does not include station-based seismic data due to the lack of local seismic stations. We also project Slab 1.0 and Slab 2.0 (solid and dashed lines in Fig. 4c) onto the vertical profile of line AA′ to augment the discussion.

From the results summarized in Fig. 4c, the Moho depth variations along the AA′ profile can be described as follows: (1) the first three stations (LALE, HUSU, and NUSU) all indicate that the Moho depth is at approximately 25 km; (2) behind the location where the Slab 1.0 and Slab 2.0 models start to change their dip angles, three stations (MARA, SEGE, and RIGN; black triangles in Fig. 4c) yield a deeper Moho depth (35–40 km); (3) at the last station (RORO), the Moho depth returns to 25 km. We first focus on the four stations behind the location where the subduction angle changes: the three stations (MARA, SEGE, and RIGN) that have a greater Moho depth reveal a large portion of the LVZ above the Moho (Fig. S5); in contrast, RORO does not present such an LVZ. The other three stations (LALE, HUSU, and NUSU) also do not display such LVZs above the picked Moho depths but only at shallower depths (Fig. S5). Note that we invert the 1-D velocity model beneath each station without much prior knowledge and consider the thickness setting of the initial model; the thickness of the LVZ might not be consistent with reality. However, our results from the data-driven inversion should be a suitable tool to examine the differences in the seismic velocity structure between the stations. The sediments and upper crust carry a large amount of water, which will be expelled from the subducting crust and sediments when the temperature increases. The released water may reduce the elastic wave velocity at shallower depths, as we observe beneath several stations (e.g., HUSU and LALE; Fig. S5).

Furthermore, the deeper Moho beneath three stations (MARA, SEGE, and RIGN) can be interpreted in terms of crustal growth due to the subduction-related magmatism (Stern and Scholl, 2010), and the LVZs observed above the deeper Moho may be explained by the lower crustal magma (Dufek and Bergantz, 2005). However, RORO, which is only a few kilometers away, does not show similar results, and more data are needed to investigate it. Based on the above discussion, we suggest that the average Moho depth is approximately 25 km around the region, but some stations have deeper Moho (35–40 km) that might be affected by subduction processes.

In addition, the seismic velocity structure beneath LALE is the most complicated compared to that of the other stations. The location of LALE is only a few kilometers away from the trench where the slab starts subducting, and the Simbo Ridge is nearby (Fig. 1). We suggest that the complex structure includes the trench, slab, and marine ridge to produce the complicated velocity model beneath LALE. We also find LVZs below the Moho beneath some stations (LALE and HUSU). Previous studies have indicated that a significant amount of serpentinite in the underlying mantle wedge could also reduce the elastic wave velocity (e.g., Ulmer and Trommsdorff, 1995; Bostock et al., 2002). Much of the water is driven off at shallow depths; however, sufficient water is released at the subcrustal level to hydrate the mantle. Metasomatism of the depleted peridotite stabilizes a variety of hydrous serpentinite. However, the serpentinite is more stable in the upper mantle at temperatures below 720 ∘C (Ulmer and Trommsdorff, 1995; Hyndman and Peacock, 2003) and becomes unstable in the arc and back-arc where the temperature in the upper mantle is more than 800 ∘C. Thus, more data, such as geochemical data or ambient thermal models, are required to determine the reason for the LVZs observed below the Moho.

Our broadband seismic network monitoring in the Western Solomon Islands started in 2009. Because the stations are deployed on the islands, it is challenging to expand our network rapidly and to perform subsequent maintenance compared to networks deployed in continental areas. However, the site survey and installation of this network are still in progress. Although records from only seven broadband seismic stations are used in this study, it provides the opportunity to examine more details about the seismic structure beneath the stations. This study provides preliminary station-based velocity models from joint inversion, and denser coverage of broadband seismic stations will be needed to integrate a 3-D velocity model for the region.

6. Conclusions

We analyze the seismograms of teleseismic events recorded at seven broadband seismic stations deployed in the Western Solomon Islands. We process the data carefully with P-wave receiver functions and Rayleigh-wave group velocity dispersion curves. The 1-D velocity models beneath the seven stations are estimated from joint inversion of the receiver functions and dispersion curves. The resulting velocity model beneath each station shows a highly variable crustal structure across the Western Solomon Islands. LVZs are observed beneath most stations except for NUSU. The Moho depth is approximately 25 km beneath four stations (LALE, HUSU, NUSU, and RORO), but the other three stations (MARA, RIGN, and SEGE) reveal a deeper Moho depths (35–40 km), which might be due to subduction processes. Other data are needed to complete the investigation of the structure; our results provide preliminary station-based velocity models for the region, which can be used in further seismological studies and jointly integrated into a 3-D velocity model in the future.

CRediT authorship contribution statement

Chin-Shang Ku: Methodology, Software, Validation, Investigation, Writing - original draft. **Yu-Ting Kuo:** Methodology, Software, Validation, Investigation. **Bor-Shouh Huang:** Investigation, Supervision. **Yue-Gau Chen:** Investigation, Supervision. **Yih-Min Wu:** Conceptualization, Methodology, Writing - review & editing, Supervision.

Declaration of Competing Interest

The authors declare that they have no known competing financial interests or personal relationships that could have appeared to influence the work reported in this paper.

Acknowledgements

The instruments used in this study provided by the Taiwan Earthquake Research Center Instrument Pool (TECIP) and the Institute of Earth Sciences (IES), Academia Sinica, Taiwan. The authors are grateful to the Seismology Section of the Ministry of Mines, Energy, and Rural Electrification of the Solomon Islands; and the Kolombangara Forest Products Limited for the support in the Western province. The authors thank Herrmann (2013) for Computer Programs in Seismology (CPS) that was used in data processing, Wessel and Smith (1998) for the Generic Mapping Tool (GMT) software, and Hunter (2007) for the Matplotlib software that were used in plotting figures. The authors thank T. C. Chi, H. L. Wang, C. M. Lin, T. L. Tseng, W. G. Huang and F. W. Taylor for their comments and discussion. We also thank Alison K. Papabatu, James Tsai, and Richard Lo for their help with fieldwork. The authors gratefully acknowledge the Ministry of Science and Technology (MOST), Taiwan to sponsor the project, under which this study was carried out (MOST-105-2116-M-002-030-MY3, MOST-108-2116-M-001-010-MY3, MOST-108-2116-M-001-026-, MOST-108-2119-M-001-019-, and MOST-106-2116-M-002-019-MY3). Our work was also supported by the Research Center of Future Earth of the National Taiwan University (NTU). This work was also financially supported by the NTU Research Center for Future Earth from the Featured Areas Research Center Program within the framework of the Higher Education Sprout Project by the Ministry of Education (MOE) in Taiwan.

Appendix A. Supplementary material

Supplementary data to this article can be found online at https://doi.org/10.1016/j.jseaes.2020.104378.

References

Acton, C.E., Priestley, K., Mitra, S., Gaur, V.K., 2011. Crustal structure of the Darjeeling-Sikkim Himalaya and southern Tibet. Geophys. J. Int. 184, 829–852. https://doi.org/10.1111/j.1365-246X.2010.04868.x.

Ammon, C.J., Randall, G.E., Zandt, G., 1990. On the nonuniqueness of receiver function inversions. J. Geophys. Res. 95, 15303–15318. https://doi.org/10.1029/jb095ib10p15303.

Bostock, M.G., Hyndman, R.D., Rondenay, S., Peacock, S.M., 2002. An inverted continental moho and serpentinization of the forearc mantle. Nature 417, 536–538. https://doi.org/10.1038/417536a.

Bodin, T., Sambridge, M., Tkalčić, H., Arroucau, P., Gallagher, K., Rawlinson, N., 2012. Transdimensional inversion of receiver functions and surface wave dispersion. J. Geophys. Res. Solid Earth 117, 1–24. https://doi.org/10.1029/2011JB008560.

Boynton, C.H., Westbrook, G.K., Bott, M.H.P., Long, R.E., 1979. A seismic refraction investigation of crustal structure beneath the Lesser Antilles island arc. Geophys. J. R. Astron. Soc. 58, 371–393. https://doi.org/10.1111/j.1365-246X.1979.tb01031.x.

Cassidy, J.F., 1992. Numerical experiments in broadband receiver function analysis. Bull. Seismol. Soc. Am. 82, 1453–1474.

Chen, T., Newman, A.V., Feng, L., Fritz, H.M., 2009. Slip distribution from the 1 April 2007 Solomon Islands earthquake: a unique image of near-trench rupture. Geophys. Res. Lett. 36, 6–11. https://doi.org/10.1029/2009GL039496.

Chen, Y., Niu, F., 2016. Joint inversion of receiver functions and surface waves with ebhanced preconditioning on densly distributed CNDSN stations: Crustal and upper mantle structure beneath China. J. Geophys. Res.: Solid Earth 121, 743–766. https://doi.org/10.1002/2015JB012450.

Corchete, V., Chourak, M., Hussein, H.M., 2007. Shear wave velocity structure of the sinai peninsula from rayleigh wave analysis. Surv. Geophys. 28, 299–324. https://doi.org/10.1007/s10712-007-9027-6.

Dufek, J., Bergantz, G.W., 2005. Lower crustal magma genesis and preservation: a stochastic framework for the evaluation of basalt-crust interaction. J. Petrol. 46, 2167–2195. https://doi.org/10.1093/petrology/egi049.

Dziewonski, A.M., Bloch, S., Landisman, M., 1969. A technique for the analysis of transient seismic signals. Bull. Seismol. Soc. Am. 59, 427–444.

Dziewonski, A.M., Anderson, D.L., 1981. Preliminary reference Earth model. Phys. Earth Planet. Inter. 25, 297–356.

Ewing, J.I., Ludwig, W.J., Ewing, M., Eittreim, S.L., 1971. Structure of the Scotia Sea and Falkland Plateau. J. Geophys. Res. 76, 7118–7137. https://doi.org/10.1029/jb076i029p07118.

Fritz, H.M., Kalligeris, N., 2008. Ancestral heritage saves tribes during 1 April 2007 Solomon Islands tsunami. Geophys. Res. Lett. 35, 1–5. https://doi.org/10.1029/2007GL031654.

Gilligan, A., Bastow, I.D., Darbyshire, F.A., 2016. Seismological structure of the 1.8 Ga Trans-Hudson Orogen of North America. Geochem. Geophys. Geosyst. 17, 2421–2433. https://doi.org/10.1002/2016GC006419.

Gilligan, A., Priestley, K.F., Roecker, S.W., Levin, V., Rai, S.S., 2015. The crustal structure of the western Himalayas and Tibet. J. Geophys. Res.: Solid Earth 3946–3964. https://doi.org/10.1002/2015JB011891.Received.

Hayes, G.P., Moore, G.L., Portner, D.E., Hearne, M., Flamme, H., Furtney, M., Smoczyk, G. M., 2018. Slab2, a comprehensive subduction zone geometry model, Science 362, 58–61. https://doi.org/10/1126/science.aat4723.

Hayes, G.P., Wald, D.J., Johnson, R.L., 2012. Slab1.0: A three-dimensional model of global subduction zone geometries. J. Geophys. Res. Solid Earth 117, 1–15. https://doi.org/10.1029/2011JB008524.

Herrmann, R.B., 2013. Computer programs in seismology: an evolving tool for instruction and research. Seismol. Res. Lett. 84, 1081–1088. https://doi.org/10.1785/0220110096.

Herrmann, R.B., Ammon, C.J., Julia, J., 2000. Joint Inversion of Receiver Functions and Surface-Wave Dispersion for Crustal Structure. Conf. Pap. 11.

Hunter, J.D., 2007. Matplotlib: A 2D graphics environment. IEEE Computer Soc. 9, 90–95. https://doi.org/10.1109/MCSE.2007.55.

Hyndman, R.D., Peacock, S.M., 2003. Serpentinization of the forearc mantle. Earth Planet. Sci. Lett. 212, 417–432. https://doi.org/10.1016/S0012-821X(03)00263-2.

Janiszewski, H.A., Abers, G.A., Shillington, D.J., Calkins, J.A., 2013. Crustal structure along the Aleutian island arc: New insights from receiver functions constrained by active-source data. Geochem. Geophys. Geosyst. 14, 2977–2992. https://doi.org/10.1002/ggge.20211.

Julià, J., Ammon, C.J., Herrmann, R.B., 2003. Lithospheric structure of the Arabian Shield from the joint inversion of receiver functions and surface-wave group velocities. Tectonophysics 371, 1–21. https://doi.org/10.1016/S0040-1951(03)00196-3.

Julià, J., Ammon, C.J., Herrmann, R.B., Correig, A.M., 2000. Joint inversion of receiver function and surface wave dispersion observations. Geophys. J. Int. 143, 99–112. https://doi.org/10.1046/j.1365-246X.2000.00217.x.

Kennett, B.L.N., Engdahl, E.R., 1991. Traveltimes for global earthquake location and phase identification. Geophys. J. Int. 105, 429–465. https://dot.org/10.1111/j.1365-246X.1991.tb06724.x.

Ku, C., Kuo, Y., Chao, W., You, S., Huang, B., Chen, Y., Taylor, F.W., Wu, Y., 2018. A First-Layered Crustal Velocity Model for the Western Solomon Islands: Inversion of the Measured Group Velocity of Surface Waves Using Ambient Noise. Seismol. Res. Lett. 89, 2274–2283. https://doi.org/10.1785/0220180126.

Kuo, Y.T., Ku, C.S., Chen, Y.G., Wang, Y., Lin, Y.N.N., Chuang, R.Y., Hsu, Y.J., Taylor, F.W., Huang, B.S., Tung, H., 2016. Characteristics on fault coupling along the Solomon megathrust based on GPS observations from 2011 to 2014. Geophys. Res. Lett. 43, 8519–8526. https://doi.org/10.1002/2016GL070188.

Langston, C.A., 1979. Structure under Mount Rainier, Washington, inferred from teleseismic body waves. J. Geophys. Res. 84, 4749–4762. https://doi.org/10.1029/JB084iB09p04749.

Laske, G., Maters, G., Ma, Z,, Pasyanos, M., 2013. Update on CRUST 1.0: a 1-degree global model of Earth's crust, Geophys. Res. Abstr. 15, EGU2013-2658. < https://ui.adsabs.harvard.edu/abs/2013EGUGA..15.2658L > .

Ligorría, J.P., Ammon, C.J., 1999. Iterative deconvolution and receiver-function estimation. Bull. Seismol. Soc. Am. 89, 1395–1400. https://doi.org/10.1016/S0304-3940(97)00816-1.

Miyagi, Y., Ozawa, T., Shimada, M., 2009. Crustal deformation associated with an M8.1 earthquake in the Solomon Islands, detected by ALOS/PALSAR. Earth Planet. Sci. Lett. 287, 385–391. https://doi.org/10.1016/j.epsl.2009.08.022.

Newman, A.V., Feng, L., Fritz, H.M., Lifton, Z.M., Kalligeris, N., Wei, Y., 2011. The energetic 2010 Mw 7.1 Solomon Islands tsunami earthquake. Geophys. J. Int. 186, 775–781. https://doi.org/10.1111/j.1365-246X.2011.05057.x.

Owens, T.J., Crosson, R.S., Hendrickson, M.A., 1988. Constraints on the subduction geometry beneath western Washington from broadband teleseismic waveform modeling. Bull. - Seismol. Soc. Am. 78, 1319–1334.

Park, J., Levin, V., 2000. Receiver functions from multiple-taper spectral correlation Estimates. Bull. Seismol. Soc. Am. 90, 1507–1520. https://doi.org/10.1785/0119990122.

Rai, S.S., Priestley, K., Gaur, V.K., Mitra, S., Singh, M.P., Searle, M., 2006. Configuration of the Indian Moho beneath the NW Himalaya and Ladakh. Geophys. Res. Lett. 33, 3–7. https://doi.org/10.1029/2006GL026076.

Sambridge, M., 1999. Sambridge-1999-Geophysical_Journal_International. Geophys. J. Int. 138, 479–494.

Schlaphorst, D., Melekhova, E., Kendall, J.M., Blundy, J., Latchman, J.L., 2018. Probing layered arc crust in the Lesser Antilles using receiver functions. R. Soc. Open Sci. 5. https://doi.org/10.1098/rsos.180764.

Shen, W., Ritzwoller, M.H., Schulte-Pelkum, V., Lin, F.C., 2012. Joint inversion of surface wave dispersion and receiver functions: a Bayesianmonte-Carlo approach. Geophys. J. Int. 192, 807–836. https://doi.org/10.1093/gji/ggs050.

Shibutani, T., Sambridge, M., Kennett, B., 1996. Genetic algorithm inversion for receiver functions with application to crust and uppermost mantle structure beneath Eastern Australia. Geophys. Res. Lett. 23, 1829–1832. https://doi.org/10.1029/96GL01671.

Stern, R.J., Scholl, D.W., 2010. Yin and yang of continental crust creation and destruction by plate tectonic processes. Int. Geol. Rev. 52, 1–31. https://doi.org/10.1080/00206810903332322.

Taylor, F.W., Briggs, R.W., Frohlich, C., Brown, A., Hornbach, M., Papabatu, A.K., Meltzner, A.J., Billy, D., 2008. Rupture across arc segment and plate boundaries in the 1 April 2007 Solomons earthquake. Nat. Geosci. 1, 253–257. https://doi.org/10.1038/ngeo159.

Taylor, S.R., 1967. The origin and growth of continents. Tectonophysics 4, 17–34. https://doi.org/10.1016/0040-1951(67)90056-X.

Tkalčić, H., Chen, Y., Liu, R., Zhibin, H., Sun, L., Chan, W., 2011. Multistep modelling of teleseismic receiver functions combined with constraints from seismic tomography: Crustal structure beneath southeast China. Geophys. J. Int. 187, 303–326. https://doi.org/10.1111/j.1365-246X.2011.05132.x.

Tetreault, J.L., Buiter, S.J.H., 2014. Future accreted terranes: a compilation of island arcs, oceanic plateaus, submarine ridges, seamounts, and continental fragments. Solid Earth 5, 1243–1275. https://doi.org/10.5194/se-5-1243-2014.

Ulmer, P., Trommsdorff, V., 1995. Serpentine stability to mantle depths and subduction-related magmatism. Science 80 (268), 858–861. https://doi.org/10.1126/science.268.5212.858.

Wang, X., Wei, S., Wang, Y., Maung Maung, P., Hubbard, J., Banerjee, P., Huang, B.S., Moe Oo, K., Bodin, T., Foster, A., Almeida, R., 2019. A 3-D Shear Wave Velocity Model for Myanmar Region. J. Geophys. Res. Solid Earth 124, 504–526. https://doi.org/10.1029/2018JB016622.

Wessel, P., Smith, W.H.F., 1998. New, improved version of Generic Mapping Tools released. Eos Trans. AGU 79, 579. https://doi.org/10.1029/98EO00426.

Zhu, L., Kanamori, H., 2000. Moho depth variation in southern California from teleseismic receiver functions. J. Geophys. Res. 105 (B2), 2969–2980. https://doi.org/10.1029/1999JB900322.